

Exploring tidal dissipation in rubble pile binary secondaries using a discrete element model

Ethan R. Burnett*, Iosto Fodde† and Fabio Ferrari‡

Abstract

In this work, models of rubble pile binary secondaries are simulated in different spin states in a system similar in size and scale to Didymos–Dimorphos. The numerical modeling is performed in the N-body Chrono-based software GRAINS, which simulates gravity, contact, and friction forces acting on non-spherical mass elements. Tidal dissipation successfully emerges in the simulations as an aggregate of the effects of inter-element contact and friction across thousands of simulated mass elements. We devise computational techniques for simulating and studying such systems, establishing rigorous numerical procedures for computing tidal quantities of interest. We compute $Q/k_2 \sim 43.5_{-27.2}^{+36.0}$ for the secondary, smaller than previously predicted ranges $10^2 < Q/k_2 < 10^6$, and thus a rather dissipative result. From our simulations, we observe non-classical variation of the tidal lag angle with the topographic longitude, and dependence of Q/k_2 on the rotation rate. Further study is required to see if the enhanced dissipativity holds with other geometries and regolith properties.

1 Introduction

Asteroids are abundant small primordial rocky worlds, leftovers from the earliest days of the solar system. Understanding their composition, morphology, and physical properties is key to understanding the origin and evolution of the rocky planets. Some large asteroids regularly cross paths with Earth. Due to the long-term risk of collision, improved understanding of their dynamical evolution could also even be necessary for ensuring the long-term survival of human civilization. In its upcoming 2029 close encounter with Earth, the $\sim 375\text{m}$ -wide asteroid (99942) Apophis will dip to within about 5 Earth radii of the Earth’s surface (significantly closer than the Moon), and will be visible to the naked eye, serving as a dramatic example of the need to track these objects and accurately predict their future paths. Multiple forces govern their dynamical evolution, beyond the familiar gravitational pull of the sun and planets. The Yarkovsky–O’Keefe–Radzievskii–Paddack (“YORP”) effect (Rubincam, 2000; Bottke et al., 2002), a thermal radiation effect, affects spin and orbital evolution via unbalanced torque and force. These bodies are also strongly affected by tidal forces, which can occur during close encounters with planets. The tidal response of these bodies in particular is poorly understood. Unlike planets and moons, these bodies are “rubble piles”, highly fractured into individual boulders held together by gravity and perhaps other forces, as opposed to the continuous rheology of larger bodies. There is no complete theory governing the tidal response of such bodies.

*Marie Skłodowska-Curie Postdoctoral Fellow, Department of Aerospace Science and Technology, Politecnico di Milano, ethanryan.burnett@polimi.it

†Postdoctoral Researcher, Department of Aerospace Science and Technology, Politecnico di Milano

‡Associate Professor, Department of Aerospace Science and Technology, Politecnico di Milano

Interestingly, $\sim 15\%$ of asteroids are binary pairs (Pravec et al., 2006). In many cases, the primary is spinning fairly quickly, and leading theories suggest that the smaller secondaries are formed from the material of the primary via binary fission (Scheeres, 2007) or by re-accretion following a mass-shedding event (Walsh et al., 2012; Wimarsson et al., 2024). Binary systems are an arena for the interaction of many complex natural forces. There is the gravitational attraction between the two bodies, which are often separated by just a few radii, so non-spherical shape effects are important, introducing strong orbit-attitude coupling effects (Hou et al., 2017). Additionally the YORP effect is still important (Holsapple, 2010), along with the so-called binary YORP (“BYORP”), which can affect the orbital evolution of the secondary, driving it further from, or even closer to, the primary (Ćuk & Burns, 2005). Most of the time these binary systems are “singly synchronous” – the secondary’s spin period matches its orbital period, thus always showing the same face towards the primary (Pravec et al., 2016). This suggests that the process by which spin energy is dissipated in binary secondaries tends to take place very quickly in comparison to the lifetime of these systems. Even in the case of the comparatively uncommon asynchronous binaries, a lot of the time they are widely separated, the end result of what is thought to be a complex chain of BYORP then YORP-driven dynamical evolution initiated by early tidal locking (Jacobson et al., 2013). Nonetheless there are also a few “tight” asynchronous binaries, with relatively small separation of primary and secondary. In these rare cases, their shape, composition, or recent encounters could have played a role in the unsettled spin states. We don’t know for sure, because tidal theory for asteroids is in a low state of development.

This work discloses results from recent numerical studies using a discrete element model to explore tidal dynamics in binary asteroid systems, as well as in flyby scenarios (E. Burnett et al., 2024; E. R. Burnett et al., 2024). The goal of this work is to develop tools and techniques to discern quantitatively how dissipative binary secondaries are in binary asteroid systems. There are many past works that are relevant to this. Pravec et al. (2016) gives a nice survey of binary secondary rotation states. Hestroffer et al. (2019) reviews the numerical and experimental research carried out recently in an effort to study rubble pile asteroids. We also refer the reader to the basics of viscoelastic tidal theory as discussed in Murray & Dermott (1999) and references therein. While binary asteroid dynamics are governed by granular mechanics, the de-facto prevailing assumption in the scientific community is that in bulk, these bodies can be approximated by the same first-order viscoelastic tidal theory used to describe the tidal evolution of planets and moons. Along this line of thought, Nimmo & Matsuyama (2019) and Goldreich & Sari (2009) derive, from first principals and order-of-magnitude analysis, effective quality factors Q and rigidity μ for rubble pile asteroids. In the realm of numerical modeling, Frouard et al. (2016) constructs an N -body damped “spring-mass” model of a planet to explore fundamentals of viscoelastic tidal theory, also discussing how the model is to be tuned to emulate realistic rheologies. Recently, DellaGiustina et al. (2024) simulates a rubble pile binary system using a discrete element model, and notes the emergence of time-varying tidal strain in the primary, computing also a tidal quality factor Q , as part of a longer work demonstrating the detectability of tidal distortions on the primary body using modern seismometers. That study is conducted using the N -body collisional code `pkdgrav` (Richardson et al., 2011), based on 1500 spherical constituent particles for the primary and 500 for the secondary. Our work is conducted in `GRAINS`, a Chrono-based N -body simulation architecture, simulating nonspherical mass elements, that has successfully been used for past studies of rubble pile asteroid morphology and dynamics (Ferrari et al., 2017; 2020; Tasora et al., 2016). Note in this work we use the terms “ N -body” and “discrete element” synonymously, but when discussing past work we use the authors’ own preferred terminology.

This work appears between the DART and Hera missions to the Didymos-Dimorphos binary as-

teroid system. On September 26, 2022, the DART spacecraft hit the smaller secondary, Dimorphos, at a speed of 6.6 km/s (Daly et al., 2024), the immediate aftermath of which was observed by both the nearby Italian LICIACube spacecraft and also by ground-based telescopes. The impact was sufficient to generate a reduction of Dimorphos’ originally ~ 12 hr orbit period by about 33 minutes (Thomas et al., 2023), and the resulting momentum deflection efficiency, ejecta cone geometry, and ejected mass provided a lot of useful information, such as constraints on the bulk strength and density of Dimorphos (Raducan et al., 2024). Agrusa et al. (2021) studied the types of attitude instabilities that could result from the DART impact, and Raducan et al. (2024) noted that based on simulations, the DART impact likely caused global deformation and resurfacing of Dimorphos. Recently Pravec et al. (2024) was able to make some constraints on the post-DART spin state of Dimorphos via lightcurve analysis. The upcoming Hera mission will provide further information about the reshaping from DART, the changes to Dimorphos’ spin (Michel et al., 2022), and from this, there could be some constraints on the dissipativity of Dimorphos.

The novel contribution of this work is to provide a numerical recipe for studying tidal dissipation in binary rubble pile systems via numerical simulation in discrete element routines. We apply this to disturbed secondaries in spin states of super-synchronous spin (i.e., an object spins faster than it revolves) or non-principal axis rotation (i.e., an object is in a drastically different spin state from the classically stable spin about the maximum principal axis). These cases have relevance to the early history of such bodies before their tidal locking, or the aftermath of collisions such as that of the DART mission. The work is conducted in GRAINS, which has some advantages over traditional spherical particle-based methods, due to the ability to capture interlocking effects due to non-sphericity of the constituent particles (Ferrari et al., 2017; 2020). The focus on the secondary allows us to achieve as small a particle size as possible for a given particle “budget”. Furthermore it affords the benefit of being able to infer Q/k_2 from the evolution of attitude dynamics, as opposed to the slower and more complex orbital dynamics. This is necessary because the numerical overhead of GRAINS presently precludes long-term orbital mechanics studies. We successfully directly observe the tidal bulge traversing the surface of the binary secondary, and furthermore we characterize the temporal lag due to dissipativity. We are also able to directly recover the resultant tidal torques, which are used to provide the first direct measurement of tidal dissipativity, in the form of Q/k_2 , for a rubble pile secondary in a numerical model of a binary system.

2 Methods

2.1 GRAINS Background

The simulations performed for this work are conducted in GRAINS, a Chrono-based N -body simulation architecture developed at the Politecnico di Milano. GRAINS models gravitational, contact, and friction dynamics between discretized non-spherical mass elements. Previously it has been used to study the aggregation of rubble piles from boulder fields (Ferrari et al., 2017; 2020), formation of binary secondaries after rotational failure (Wimarsson et al., 2024), shape equilibrium of rubble piles (Ferrari & Tanga, 2022), and the dynamical evolution of the Didymos-Dimorphos binary asteroid system post-impact (Agrusa et al., 2022; Ferrari et al., 2022). There are also a number of other studies of rubble pile asteroid systems currently ongoing. In this work, we simulate the motion of a rubble pile secondary in binary asteroid systems similar to the Dimorphos-Didymos system in size and scale, but the secondary is initialized in highly non-equilibrium spin states to induce and study more pronounced dynamic tidal effects in young, unsettled (or otherwise perturbed) binary asteroid systems. We use the pre-impact shape of Dimorphos for lack of a good

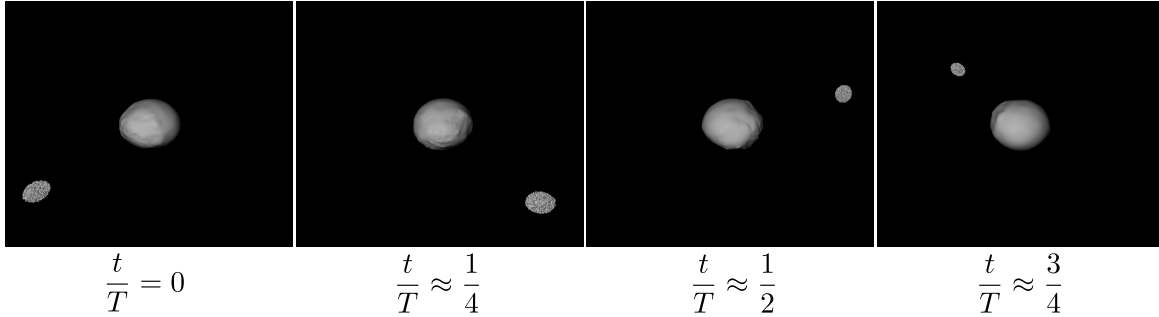


Figure 1: A binary asteroid simulation in GRAINS. The spin state of the secondary is initialized with sufficient angular velocity to yield bounded but significant yaw from the minimum-energy attitude (where the long axis is collinear with the orbit radial direction). The notation $t/T \approx \frac{1}{4}$ means that roughly one-fourth of an orbit is completed.

post-impact model. Due to runtime considerations and a focus on the attitude dynamics of the secondary, the primary is modeled with point-mass gravity and the numerical budget of discrete mass elements is devoted to modeling the secondary. Details of the model and various considerations are discussed as needed in the sections that follow. A visual depiction of one orbit from an example GRAINS simulation of the binary system is provided in Figure 1. In our studies we model rubble pile secondaries in a range of ~ 1700 -3000 elements, and this particular model is on the low end of that range. The “ t/T ” notation, used frequently in this work, is a non-dimensional representation of time in terms of Dimorphos orbit periods.

2.2 Building a numerical tidal physics “sandbox”

2.2.1 Orientation and frames

We start by defining the orbit frame $\mathcal{O}' = \{-\hat{e}_r, -\hat{e}_t, \hat{e}_h\}$, where $\hat{e}_r = \mathbf{r}/r$ is the unit vector pointing from primary to secondary centers of mass, \hat{e}_h points in the orbital angular momentum direction, and \hat{e}_t completes the right-handed triad and points roughly along the orbital velocity direction. Next, the principal axis frame \mathcal{B} diagonalizes the inertia tensor into $\text{diag}(A, B, C)$ for principal moments of inertia (MoI) $C \geq B \geq A$. We denote rotations from one reference frame “ \mathcal{A} ” to another “ \mathcal{B} ” as $[\mathcal{B}\mathcal{A}]$. Where needed, vectors are resolved in a particular frame, e.g. ${}^{\mathcal{B}}\mathbf{r}$. In this work we make use of a yaw-pitch-roll attitude formulation with respective angles ψ, θ, ϕ defined below in terms of components of the rotation matrix $[\mathcal{B}\mathcal{O}']$:

$$\psi = \text{atan2}(\mathcal{B}\mathcal{O}'_{1,2}, \mathcal{B}\mathcal{O}'_{1,1}) \quad (1a)$$

$$\theta = \sin^{-1}(\mathcal{B}\mathcal{O}'_{1,3}) \quad (1b)$$

$$\phi = \text{atan2}(\mathcal{B}\mathcal{O}'_{2,3}, \mathcal{B}\mathcal{O}'_{3,3}) \quad (1c)$$

Thus $\psi = \theta = \phi = 0$ denotes the case of the long axis pointing towards the primary, with all three principal axes parallel to a basis vector of \mathcal{O}' . The body frame definition is depicted in Fig. 2. This choice renders counter-clockwise super-synchronous rotation to have positive sign $\psi > 0$ for consistency with foundational literature on spin and tides (Murray & Dermott, 1999; Goldreich & Peale, 1966). We also define an arbitrary inertial frame \mathcal{N} , fixed with respect to the stars, in which the calculations of GRAINS are generally conducted.

Because the rubble pile secondary is not a rigid body, the topography is not fixed in the principal axis frame \mathcal{B} . For simulations with super-synchronous rotation, we observe some longitudinal

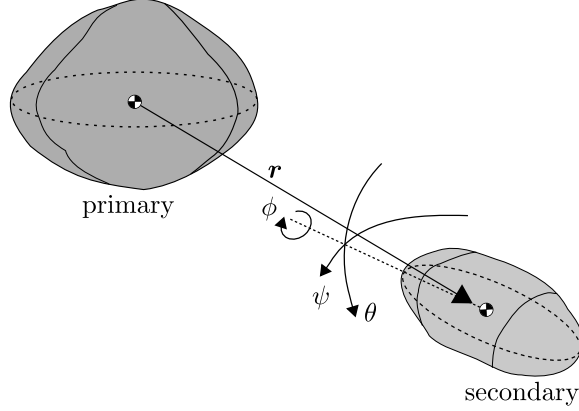


Figure 2: Asteroid orientation showing the Euler angle sequence ψ, θ, ϕ describing the 3-2-1 rotation from orbit frame \mathcal{O}' to a body frame \mathcal{B} .

oscillation of the topography in this frame. To facilitate easy topographical studies, an alternate body frame definition is now discussed. Noting that the deep interior of the asteroid has greatly reduced rock movement in comparison to the shallower depths, due to increased overburden pressure (Nimmo & Matsuyama, 2019), a “topography-fixed” frame \mathcal{G} can be defined, in which the location of select rocks deep in the interior is fixed by definition. Being careful to exclude any of the few deep interior mass elements that undergo appreciable migration or settling, a basis is constructed of the position of at least three satisfactory elements via the following process. First, the coefficient vectors are computed:

$$W_\star = [\mathcal{N}\delta\hat{\mathbf{r}}^1(t_\star) \quad \mathcal{N}\delta\hat{\mathbf{r}}^2(t_\star) \quad \mathcal{N}\delta\hat{\mathbf{r}}^3(t_\star)] \quad (2)$$

$$\boldsymbol{\alpha} = W_e^{-1}[\mathcal{B}\mathcal{N}_e]^\top \hat{\mathbf{e}}_1 \quad (3a)$$

$$\boldsymbol{\beta} = W_e^{-1}[\mathcal{B}\mathcal{N}_e]^\top \hat{\mathbf{e}}_2 \quad (3b)$$

$$\boldsymbol{\gamma} = W_e^{-1}[\mathcal{B}\mathcal{N}_e]^\top \hat{\mathbf{e}}_3 \quad (3c)$$

where in this context $\hat{\cdot}$ denotes a vector of unit norm, the $\hat{\mathbf{e}}_i$ are basis vectors e.g. $\hat{\mathbf{e}}_1 = (1, 0, 0)^\top$, and otherwise subscripts $(\cdot)_\star = (\cdot)(t_\star)$ indicate evaluation of a quantity at a specified time t_\star , the time t_e is specifically the *epoch time*, and $\delta\hat{\mathbf{r}}^i = (\mathbf{r}^i - \mathbf{r})/(\|\mathbf{r}^i - \mathbf{r}\|)$ is the vector from the barycenter of the secondary to the i^{th} element. Note that elsewhere in this paper mass element indexing is typically associated with *subscripts*. Generally in this study we choose rocks at a depth of $\|\delta\mathbf{r}^i\| \leq 0.4R$. Having defined the basis vectors, the rotation can be resolved at any time $t_k \geq t_e$ as below:

$$\mathbf{g}^1(t_k) = W_k \boldsymbol{\alpha} \quad (4a)$$

$$\mathbf{g}^2(t_k) = W_k \boldsymbol{\beta} \quad (4b)$$

$$\mathbf{g}^3(t_k) = W_k \boldsymbol{\gamma} \quad (4c)$$

$$[\mathcal{GN}]_k = [\hat{\mathbf{g}}^1(t_k) \quad \hat{\mathbf{g}}^2(t_k) \quad \hat{\mathbf{g}}^3(t_k)] \quad (5)$$

$$[\mathcal{GO}'] = [\mathcal{GN}][\mathcal{ON}]^\top [\mathcal{OO}'] \quad (6)$$

$$[\mathcal{O}\mathcal{O}'] = \begin{bmatrix} -1 & 0 & 0 \\ 0 & -1 & 0 \\ 0 & 0 & 1 \end{bmatrix} \quad (7)$$

Via the computational procedure of Eqs. (2) - (7), the epoch rotation matrices $[\mathcal{G}\mathcal{O}']_e$ and $[\mathcal{B}\mathcal{O}']_e$ are the same, and the \mathcal{B} and \mathcal{G} frames are aligned at time t_e . These calculations, and really any calculations of interest, should be performed *after* any initial short transient shifting and settling behavior, i.e. we require $t_e > t_0$.

2.2.2 Initialization of the Rubble Pile

For this work, rubble pile models are constructed via the same aggregation procedure as prior GRAINS works, so the interested reader is deferred there (Ferrari et al., 2017; 2020). Initial transient behavior occurs in our simulations whenever the initial conditions of a given rotational scenario are different from the conditions that generated the original rubble pile aggregate. The differential spin disrupts the rubble pile secondary slightly from its old equilibrium, resulting in a rapid re-settling of the constituent particles. This manifests as a small “jump” in the eigenvalues of the inertia tensor, which furthermore manifests in some other plots as well. In our studies we often reuse the same model in different rotational scenarios, so the initial transience is unavoidable. This behavior is generally observed to be quite short, however, to be discussed later in the paper.

2.2.3 N-body Dynamical Modeling

We study the orbital and attitude dynamics of the rubble pile secondary in a binary asteroid system. In our numerical implementation, for timespans of interest of days to weeks, we are still limited to a few thousand particles in an N -body simulation. In lieu of splitting the budget of particles between primary and secondary, we instead opt for rendering the secondary as a rubble pile with the maximum practical resolution, and hence the primary is modeled as a single massive particle. This is appropriate for our studies which are focused specifically on dissipation within the secondary. A rough but useful perspective, assuming $M \gg m$, is that changes to the orbit of the secondary are dominated by dissipation within the primary, whereas changes in the spin state of the secondary are dominated by dissipation within the secondary (Murray & Dermott, 1999).

The dynamics at work are the result of forces of N -body gravitation, inter-element contact, and friction. The N -body potential is given below for primary mass M and mass elements dm_i , $i \in [1, N]$, neglecting the second-order terms from attraction between individual non-spherical elements:

$$U = -G \left(\sum_j \frac{M dm_j}{\delta r_j} + \sum_{1 \leq i < j \leq N} \frac{dm_i dm_j}{\delta r_{ij}} \right) \quad (8)$$

where $m = \sum_i dm_i$ is the total mass of the secondary and G is the universal gravitational constant. By default, GRAINS does not compute the gravitational effects of non-spherical moments between mass elements, to avoid prohibitive runtimes. The neglected inter-element gravitational torque effects are quite sub-dominant in comparison to contact and friction effects, however, where the non-sphericity of individual particles is very important. Further details of the dynamics model can be found in Ferrari et al. (2020). The aggregate inertia tensor of the rubble pile secondary is computed without approximation, with the positions, angular velocities, and angular momenta of all individual particles also tabulated. As a result, the total angular momentum of the system is computed and tabulated. We observe that it is approximately conserved in our simulations to a

high degree of accuracy (to be discussed – see Results), establishing the first of two tests of GRAINS physical accuracy for the binary system.

Contact is modeled using the Smooth Contact Method of Chrono. Contact is emulated via a viscoelastic model, resolving contact-normal and tangential forces as below (Tasora et al., 2016):

$$\mathbf{F}_{f,n} = K_n \delta_n^p \hat{\mathbf{n}} - \gamma_n \delta_n^q \mathbf{v}_n \quad (9a)$$

$$\mathbf{F}_{f,t} = -K_t \delta_t^s \hat{\mathbf{t}} - \gamma_t \delta_t^q \mathbf{v}_t \quad (9b)$$

where K_n and K_t denote normal and tangential components of the stiffness parameter, and γ_n and γ_t denote normal and tangential components of the damping parameter. These parameters can be computed from material properties. The contact displacement vector is $\boldsymbol{\delta} = \boldsymbol{\delta}_n + \boldsymbol{\delta}_t$, and $\hat{\mathbf{n}} = \boldsymbol{\delta}_n / \|\boldsymbol{\delta}_n\|$ and $\hat{\mathbf{t}} = \boldsymbol{\delta}_t / \|\boldsymbol{\delta}_t\|$ are the unit directions. Finally \mathbf{v}_n and \mathbf{v}_t denote the normal and tangential components of the velocity vector. For the Hertz contact model, $p = 3/2$, $q = 1/4$, and $s = 1/2$. The tangential force respects the Coulomb friction condition $\|\mathbf{F}_c\| \leq \mu \|\mathbf{F}_n\|$ for friction coefficient μ .

For further details of the contact detection and of mass element interaction modeling, the interested reader is directed to Ferrari et al. (2017), and to the references of the Chrono physics engine (Tasora et al., 2016; Fleischmann, 2015). GRAINS also has the ability to model cohesion, although cohesion forces are set to zero in this work. Each mass element in the simulation is modeled as a convex body of a maximum of 16 vertices and an average of about 10. All mass elements are of approximately the same size but differ in shape. The setup of the rubble pile secondary is similar to the GRAINS setup in Agrusa et al. (2022). Finally, the dynamics in this work neglect the spin effects of YORP (Holsapple, 2010). For our highly disturbed spin states, closely separated primary and secondary, and relatively short simulation timescales, the tidal torques will dominate. We also neglect the BYORP effect, which is important for long-term orbital evolution, but initiates only after the tidal locking of a binary secondary (Ćuk & Burns, 2005).

For a point-mass primary of mass M and a perfectly rigid secondary of mass m , the total system energy is given below:

$$E = \frac{1}{2} M v_1^2 + \frac{1}{2} m v_2^2 + \frac{1}{2} \boldsymbol{\omega}^\top I \boldsymbol{\omega} - \frac{GMm}{r} - \frac{GM}{2r^3} (A + B + C - 3\Phi(\boldsymbol{\eta})) \quad (10)$$

where I is the secondary inertia tensor, $\boldsymbol{\omega}$ is the secondary rotational angular velocity, and Φ is from a second-order expansion of the potential in MacCullagh’s approximation (Murray & Dermott, 1999):

$$\Phi(\boldsymbol{\eta}) = \frac{Ax^2 + By^2 + Cz^2}{r^2} \quad (11)$$

where the vector ${}^{\mathcal{B}}\mathbf{r} = (x, y, z)^\top$ resolves the location of the perturbing primary in the body frame of the secondary, and $r = \sqrt{x^2 + y^2 + z^2}$. For tidally locked cases with limited deformations of the binary secondary, the moments of inertia do not change much and frictional dissipation is not aggressive, and this quantity is thus approximately conserved in our simulations to a high degree of accuracy (see Results), establishing the second test of GRAINS physical accuracy. We can also isolate the *rotational energy* of the secondary, which is a function of the orientation and rotational state and distance between the two bodies:

$$\mathcal{E} = \frac{1}{2} \boldsymbol{\omega}_r^\top I \boldsymbol{\omega}_r + V(\boldsymbol{\eta}, r) \quad (12)$$

where $\boldsymbol{\omega}_r = \boldsymbol{\omega} - \boldsymbol{\omega}_{\text{orb}}$ denotes the angular velocity relative to the rotating Hill frame, and $V(\boldsymbol{\eta}, r)$ is the final term in Eq. (10). Note in the planar case where rotations are limited to the orbital plane, it takes on the familiar form $V(\psi) = -\frac{3}{4}\frac{GM}{r^3}(B - A)\cos 2\psi$ for yaw angle ψ about the body polar axis (Murray & Dermott, 1999; Goldreich & Peale, 1966). Applying the additional assumption of a circular Keplerian orbit $r = a = a_0$ and neglecting the effect of attitude on the orbit, Eq. (12) becomes a conserved quantity. In reality, the orbit is not perfectly circular, and the orbital and attitude dynamics of the binary secondary are linked. Nonetheless, for our simulations with near-circular orbits, the equation is still useful because it allows us to obtain useful approximations of limits on the orientation and rotation state of the secondary, in particular whether roll is permitted, and at a high enough energy level, whether super-synchronous rotation (SSR) is expected. Consider first the attitude case $\psi = \pm\frac{\pi}{2}$, $\theta = \phi = 0$ with $\boldsymbol{\omega}_r = \mathbf{0}$. In this case, $\Phi(\boldsymbol{\eta}) = B$, the rotational kinetic energy term in Eq. (12) is zero, and the energy for this case is given below:

$$\mathcal{E}_{\text{SSR}} = -\frac{GM}{2r^3}(A + C - 2B) \quad (13)$$

Alternatively, for the attitude case $\psi = \theta = 0$, $\phi = \pm\frac{\pi}{2}$ with $\boldsymbol{\omega}_r = \mathbf{0}$, $\Phi(\boldsymbol{\eta}) = A$, yielding the following:

$$\mathcal{E}_{\text{roll}} = -\frac{GM}{2r^3}(B + C - 2A) \quad (14)$$

Starting with some initial orientation $\boldsymbol{\eta}(0)$ and spin $\boldsymbol{\omega}_r(0)$, the value of the resulting rotational energy \mathcal{E} relative to the critical values \mathcal{E}_{SSR} and $\mathcal{E}_{\text{roll}}$ provides limitations on the resulting qualitative behavior that is possible due to conservation of the rotational energy. Namely, roll is possible when $\mathcal{E} > \mathcal{E}_{\text{roll}}$, and not possible when $\mathcal{E} \leq \mathcal{E}_{\text{roll}}$. Similarly, super-synchronous rotation is possible when $\mathcal{E} > \mathcal{E}_{\text{SSR}}$, whereas tidal locking is expected when $\mathcal{E} \leq \mathcal{E}_{\text{SSR}}$. These conclusions rely on conservation of rotational energy and neglect orbit-attitude coupling, so they do not exactly hold in the simulation results. Nonetheless they are useful approximations that we make use of when choosing initial conditions to produce a certain type of behavior. By our convention $C \geq B \geq A$, it is also true that $\mathcal{E}_{\text{SSR}} \geq \mathcal{E}_{\text{roll}}$, which makes intuitive sense.

2.2.4 Basic Tidal Theory

The total tidal torque induced by the gravitational pull of the primary on the secondary is well-approximated by the following expression derived from MacCullagh's approximation:

$$\begin{aligned} \boldsymbol{\Gamma} &= \mathbf{r} \times -\nabla V(\boldsymbol{\eta}, r) \\ &= \frac{3GM}{r^3} \mathcal{B} \hat{\mathbf{e}}_r \times I^{\mathcal{B}} \hat{\mathbf{e}}_r \end{aligned} \quad (15)$$

In the planar case where rotations are limited to the orbital plane, this reduces to below (Murray & Dermott, 1999; Goldreich & Peale, 1966):

$$\boldsymbol{\Gamma} = -\frac{3}{2}\frac{GM}{r^3}(B - A)\sin 2\psi \hat{\mathbf{e}}_h \quad (16)$$

Because GRAINS tabulates total angular momentum at every timestep for each body, the torque on the secondary can also be recovered by smoothing and differentiating the time series $\mathbf{H}_2(t)$, the rotational angular momentum of the secondary:

$$\boldsymbol{\Gamma} = \dot{\mathbf{H}}_2 = \dot{I}\boldsymbol{\omega} + I\dot{\boldsymbol{\omega}} \quad (17)$$

In our studies, the numerical disagreement between Eqs. (15) and (17) is small (see Results), and we defer to the numerically computed term for most calculations, because the differentiation error is lower than the approximation error.

The tidal torque can be split into two components: the torque due to *permanent mass asymmetry* Γ_{PMA} , and the torque due to a time-varying effect on the MoI induced by the gravitational pull of the primary, Γ_{Tidal} . On terrestrial planets, the former term is due to the gravitational torque on *static* large-scale inhomogeneities and uncompensated topographic variations (Melosh, 2011; Murray & Dermott, 1999), and the latter is due to the torque on the *dynamic* lagging transient deformation of the body from the gravitational pull of a perturber. The relative strength of these two torques determines the final spin state of the body (Goldreich & Peale, 1966). In the case of rubble pile asteroids, the body has very low effective “strength” or rigidity, held together by weak gravitational, friction, and perhaps electrostatic forces (Sánchez & Scheeres, 2014). For such low-strength granular bodies, this concept may be harder to visualize, but it still holds.

In this paper we are interested in how dissipative the rotational settling process is, by which the binary secondary achieves an equilibrium spin state from an initially disturbed state. We will explore both planar spin and tumbling cases for our initially unsettled spin states. Consider the fully planar case of supersynchronous rotation, for which ψ is unbounded. In this case, for a simple circular orbit, the rotationally averaged torque due to the permanent mass asymmetry is zero. Thus the rotationally averaged total torque is just a function of the tidal torque:

$$\bar{\Gamma}_z = \frac{1}{2\pi} \int_{-\pi}^{\pi} (\Gamma_{z,\text{PMA}}(\psi) + \Gamma_{z,\text{Tidal}}(\psi, t)) d\psi = \bar{\Gamma}_{z,\text{Tidal}} \quad (18)$$

From the GRAINS results, we compute and tabulate the total torque $\Gamma(t)$ at various times. In the case of planar spin, numerically averaging e.g. by a trapezoidal or spline method, we are also able to estimate the averaged torque, Eq. (18). In this work we directly numerically compute the tidal torque on the secondary, due to its own internal dissipation, and are not beholden to any particular tidal theory. It is however of great interest to represent the results we recover by well-known metrics in the literature.

For a measure of how dissipative the body is, we’ll start with the unimodal MacDonald model (Murray & Dermott, 1999), which is quite simplistic and not representative of realistic rheologies (Williams & Efroimsky, 2012; Efroimsky, 2012), but nonetheless the subject of popular works in planetary science and in binary asteroid studies (Nimmo & Matsuyama, 2019; Pou & Nimmo, 2024; Goldreich & Sari, 2009). Consider a damped driven unimodal oscillator of frequency ω . The oscillator’s response will always lag the driving force with some angle $-\pi < \delta \leq 0$. Over a full cycle (rotation or libration), the *quality factor* Q conveys the “quality” of this damped oscillator in retaining energy, with smaller values indicating higher dissipation (Murray & Dermott, 1999):

$$Q = \frac{2\pi\mathcal{E}_0}{\Delta\mathcal{E}} \quad (19)$$

Assuming weak damping and a system far from resonance, the phase lag is equated to the quality factor by $\sin \delta = -1/Q$. By MacDonald’s analysis (Efroimsky, 2012; Murray & Dermott, 1999), the physical lag angle of the unimodal response is $\epsilon = \delta/2$, and the torque is as below:

$$\Gamma_{\text{Tidal}} = -\frac{3}{2}k_2 \frac{GM^2}{a^6} R^5 \sin 2\epsilon \quad (20)$$

where k_2 is the (order-2) tidal *Love number* of the secondary and R is its radius (Murray & Dermott, 1999). Applying the earlier mentioned relationships of phase and physical lags and the

quality factor, the following is produced, assuming $\sin \epsilon \approx \epsilon$:

$$\Gamma_{\text{Tidal}} = -\frac{3}{2} \left(\frac{k_2}{Q} \right) \frac{GM^2}{a^6} R^5 \quad (21)$$

Note that the process by which this relationship is obtained is disputed for a variety of reasons (Williams & Efroimsky, 2012; Efroimsky, 2012). Perhaps the greatest argument against this paradigm is that the assumption of unimodal response is not physically realistic. In reality a variety of tidal modal frequencies with their corresponding tidal lags are to be expected. Nonetheless we will continue with this derivation due to its frequent use in literature. Averaging over a full rotation and equating Eqs. (18) and Eq. (21), we re-arrange to isolate Q/k_2 , itself a measure of dissipation:

$$\frac{Q}{k_2} \sim - \left(\frac{2}{3} \frac{a^6}{GM^2} R^{-5} \langle \bar{\Gamma}_z \rangle \right)^{-1} \quad (22)$$

Smaller relative values of Q/k_2 indicate more dissipative bodies. Among the numerical results from our N -body simulations, we provide computed values of Q/k_2 for the super-synchronous spin case.

For tumbling and non-principal axis rotation cases, the secondary undergoes significant changes in its angular orientation. We seek to directly compare the dissipation in disrupted non-planar spin states to the super-synchronous spin case. This is done by choice of a more general function that recovers the planar result while still applying to the 3D case. The following expression, leveraging Newton’s equation for rotational motion $\dot{\mathbf{H}} = \mathbf{\Gamma}$, recovers the result of Eq. (22) in the case of super-synchronous spin with the selection of T^* as the time for a full rotation with respect to the primary:

$$\frac{Q}{k_2} \sim - \left(\frac{2}{3} \frac{a^6}{GM^2} R^{-5} \frac{1}{T^*} (\|\mathbf{H}_2(t_0 + T^*) - \|\mathbf{H}_2(t_0)\|) \right)^{-1} \quad (23)$$

where exact equality of the two is achieved only in the case of constant SSR rate $\dot{\psi}$, but this does not introduce disagreement of more than a few percent for our studies. One further challenge is that in the tumbling case, the secondary no longer “cycles”, i.e. regularly repeating the same attitude. The choice of a suitable T^* is thus unclear, which becomes relevant later in our numerical analysis.

2.3 Capabilities and Limitations

2.3.1 Numerical modeling in GRAINS

Runtime timescales are long in N -body nonspherical granular mechanics-based simulations due to the computationally costly contact-checking operations (Ferrari et al., 2020; 2017). However, the simulation of contact between non-spherical elements allows us to simulate certain granular mechanisms resulting from non-sphericity of the constituent particles (see e.g. Ferrari & Tanga (2022) and references therein). In our current implementation of GRAINS, models of a few thousand particles typically simulate in $\sim 1/2$ -real time. Thus, for a Dimorphos-like orbit period of ~ 11 hrs, we are limited to ~ 7 orbits for studies with reasonable turn-around times of e.g. week-long simulations. However, this is enough to perform meaningful studies. Using the rotational energy equation Eq. (12) to specify reasonable starting states (say, not far above \mathcal{E}_{SSR} for the super-synchronous case) enables interesting qualitative behavioral transitions (such as spin-down) to be set up and observed.

The tracking of individual mass elements enables unique local and global studies of rock movements – settling, jostling, migration, and global tidal response. This is illustrated conceptually by

Figure 3 which depicts, for our Dimorphos-like body, the displacement of rocks in an equatorial cross-section due to tidal response in a super-synchronous spin simulation. Note that GRAINS makes use of a non-dimensional length scale (units of L) as a consequence of the methodology for accommodating specified target bulk densities. The interested reader is referred to Ferrari et al. (2017). Unless otherwise indicated, length units in this paper will be in terms of L . See Table 2 in Results for the conversion relevant for Figure 3.

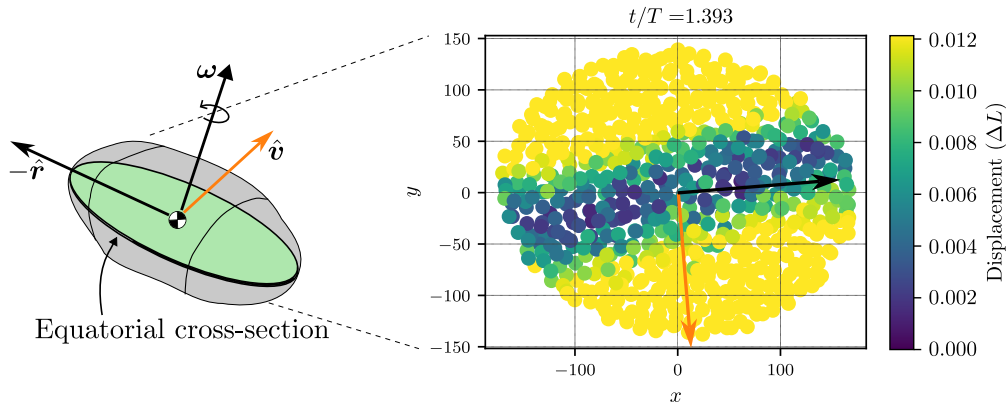


Figure 3: Modeling of each discrete element of the rubble pile enables advanced study of local and large-scale rock movements. Here, an equatorial cross-section “snapshot” displays the color-coded motion of individual grains, clearly illustrating the resultant degree-2 tidal distortion nearly aligned with the radial vector, with misalignment due to tidal lag. Note that each mass element is represented as a colored circle – our discrete element model does not use spherical mass elements.

While limited by the tradeoff between number of mass elements and simulated timespan, GRAINS is particularly well-suited to modeling rubble pile secondaries such as Dimorphos. The reasons are twofold. First, because modeling the small secondaries allows for a finer resolution (e.g. smaller boulder size) for the same number of particles in comparison to the much larger primary. Assuming a body constructed of similarly sized mass elements, individual mass elements scale in size as $R_{\text{elem}} \sim \frac{R}{N^{1/3}}$ for secondary mean radius R . Thus for a Dimorphos-like model with a few thousand elements, the resulting elements are meter-scale. Second, observed disparities in cohesive strength between Didymos and Dimorphos suggest that fine grains may be scarce in binary secondaries (Raducan et al., 2024), possibly due to fine grain escape from solar radiation pressure before its accretion (Raducan et al., 2024; Ferrari et al., 2022). Daly et al. (2023) also notes a steep drop-off in Dimorphos’ surface boulder population for boulders with $< 0.3\text{m}$ width, noting the finding is not an artifact of limits on camera resolution.

2.3.2 Tidal dissipativity

We assume that for small rubble pile secondaries such as Dimorphos, tidal dissipation is dominated by friction, in concurrence with Nimmo & Matsuyama (2019), as opposed to plastic yielding of stress concentrations due to roughness of the mass elements (e.g. Goldreich & Sari (2009)). Our reasoning is that the secondaries are small and loosely packed, so shallow mass elements can shift and rotate subject to local stresses. For mass elements not in a maximally compact configuration, contacts on stress concentrations could exert a torque on the element that overcomes the resistive torque of contact friction with neighboring elements. Thus reconfiguration and compaction can occur before plastic yielding, and this process removes energy via frictional sliding.

We’re interested in estimating the dissipativity of rubble pile binary secondaries. Cognizant of the limitations of numerical modeling, we prefer an underestimate to an overestimate. Real rubble pile binary secondaries, while possibly deficient in fine regolith, will surely have more fine regolith than our simulation with meter-scale mass elements. Classically one would expect that they should be more dissipative than our model. Colloquially, a bag of marbles is more dissipative than a single large marble of the same material and mass (Nimmo & Matsuyama, 2019). Similarly, a bag of “sand” of the same material and mass might be expected to be the most dissipative of the three. However, the relationship might not be this simple. In mixed regolith with low mass fractions \mathcal{F} of small particles, where $\mathcal{F} = m_s/(m_b + m_s)$ for small particles of total mass m_s and large particles of total mass m_b , the rigidity/shear modulus increases with \mathcal{F} until a critical point, as voids between the large particles are filled (Marti et al., 2024). This should have an overall effect of stiffening the rubble pile, reducing the thickness of the dissipative regolith layer. As the small particles begin to dominate, however, the fine regolith fraction becomes increasingly responsible for the total tidal dissipation. Thus the dissipative layer depth may decrease with finer grains, but its dissipativeness per unit volume may increase. In reality the expected dissipativeness of a rubble pile asteroid constructed from a given regolith is a complicated issue necessitating further experiments.

Finally, a few more things are worth noting. First, in this work, we explore the case of a perturbed secondary. For this case, some of the scaling laws in Nimmo & Matsuyama (2019) need to be re-derived, because they were originally derived for the case of studying dissipation in a primary by an orbiting secondary of smaller mass. We don’t include these because the modifications of the needed equations are fairly easy. Second, much of the existing tidal theory rests on the assumption that, in bulk, such bodies behave in a way that can be approximated by viscoelastic theory. However, it is more likely to say that the bulk behavior will be approximated well, within certain dynamical regimes, with linearizable (though *not necessarily classically viscoelastic*) equations with effective rigidity and viscosity, and possibly other unknown parameters (Efroimsky, 2015). Additionally, there is little work into the threshold of how many bodies (i.e. how many N in an N -body simulation) are needed to render linearizable equations well-approximated by continuum mechanics, nor the effect of the scale of N on the resulting continuum approximation.

3 Results

We provide the key results of two simulations of the attitude, orbit, and rock movements of rubble pile secondaries in non-settled attitude states. The first is a case of non-principal axis rotation (denoted “NPA”), and the second is a case of super-synchronous rotation (denoted “SSR”) in which the secondary undergoes noticeable spin-down in the course of the simulation.

3.1 Case 1: Non-principal axis rotation

Important simulation information is summarized in Table 1. The rubble pile secondary is initialized in a spin state with some significant initial nonzero yaw and roll, though not enough to initialize a super-synchronous rotation state. The resulting attitude evolution is given in terms of Euler angles in Fig. 4a and in terms of the angular velocity of the \mathcal{B} frame with respect to \mathcal{O}' in Fig. 4b. The attitude transitions from a bounded state with all angles less than 90 degrees to a state of roll (rotation about the long axis, which points towards the primary).

Fig. 4c gives the tidal torque about the x, y, z body axes of the binary secondary, as reproduced from the outputs of GRAINS. strong agreement can be noted between the numerically recovered estimate of the tidal torque (dashed lines), Eq. (17), and the computation based on MacCullagh’s

Table 1: Simulation Parameters for Case 1

Parameter	Value
Gravitational constant G	$2.2909 \times 10^{-10} \text{ kg} \cdot \text{L}^3/\text{s}^2$
Primary and secondary mass	$M = 5.35073 \times 10^{11} \text{ kg}$, $m = 4.87879 \times 10^9 \text{ kg}$
Secondary number of particles	1687
Scaling parameter	$1 \text{ m} = 1.50847 \text{ L}$
Physical properties	Young's mod. $Y = 3 \text{ GPa}$, Friction $\mu = 0.6$, Poisson $\nu = 0.3$
Initial attitude of secondary	$\psi = \theta = \phi = 0$
Initial angular velocity	$\boldsymbol{\omega}_2 = (0.8, 0, 2.2642) \times 10^{-4} \text{ rad/s}$
Initial orbit elements	$a = 1796.9\text{L}$, $e = 1.1812 \times 10^{-3}$, $f = 0^\circ$
Timescales	$T_{\text{orbit}} \approx 12.0 \text{ hrs}$, $T_{\text{libration}} \approx 12.7 \text{ hrs}$

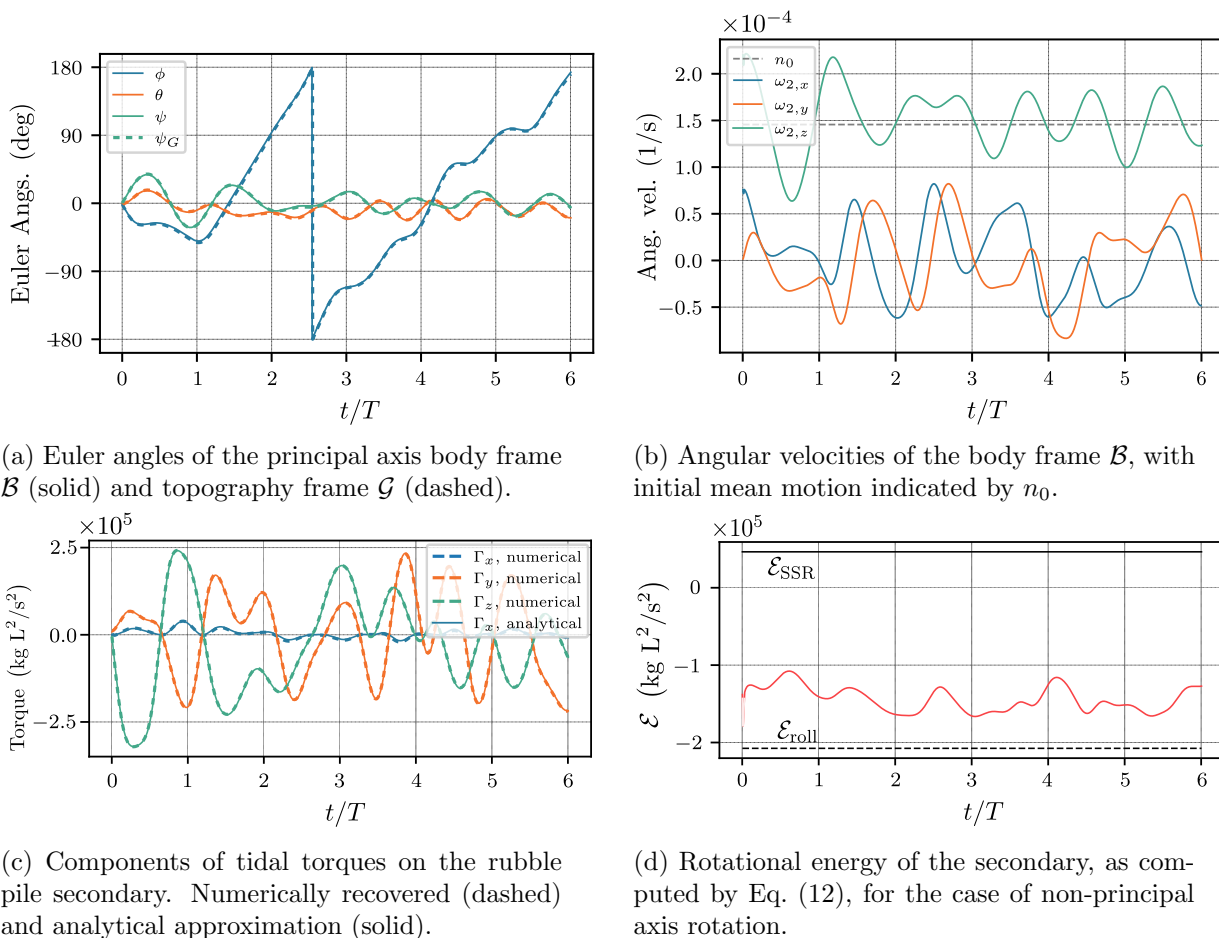


Figure 4: Simulation results for Case 1 (NPA). \mathcal{B} frame Euler angles (a) correspond to the rotation matrix $[\mathcal{B}\mathcal{O}']$, whereas \mathcal{G} corresponds to the rotation matrix $[\mathcal{G}\mathcal{O}']$. The tidal torques (c) are provided in the \mathcal{B} frame. Rotational energy (d) is insufficient to end up in a super-synchronous rotation case, as evidenced by $\mathcal{E} < \mathcal{E}_{\text{SSR}}$. Furthermore there is enough energy for roll, $\mathcal{E} > \mathcal{E}_{\text{roll}}$. Note this quantity is only an approximation and is not meant to be conserved.

approximation (solid lines), Eq. (15). Torque along the long axis (x) is quite low compared to the other two body axes. Even though the angular departures of yaw and pitch are fairly small in comparison to the unbounded roll, the torque along the body y and z axes dominates. Fig. 4d gives the rotational energy of the secondary, as computed by Eq. 12, for the case of non-principal axis rotation. The energy is sufficient to end up in a roll state, as $\mathcal{E} > \mathcal{E}_{\text{roll}}$, but not enough to end up in a supersynchronous rotation state, because $\mathcal{E} < \mathcal{E}_{\text{SSR}}$. This energy quantity, while not conserved, displays limited secular change over the course of the simulation. Initialization-based transient effects (see Section 2.2.2) create a “dip” in \mathcal{E} in the first $\sim 1/10$ of an orbit which should be ignored, as they violate the assumptions made in the derivation of \mathcal{E} . This part of the plot is thus washed-out.

Over the course of the simulation, the total system energy as approximated by Eq. (10) (a rigid-body approximation) is computed and the result is plotted in Fig. 5. This is then factored into the classical orbital energy E_O (assuming that the primary and secondary are point masses located at their respective barycenters) and the remaining energy of the secondary E_S , such that $E_O + E_S = E$. The total energy is conserved to within 0.1%, indicating that the rigid-body assumption is not a poor one for this non principal axis rotation case, and importantly, establishing that GRAINS is conserving energy to a tolerable degree of accuracy for an N -body simulation architecture. Again this energy quantity displays a brief dip in the beginning due to initialization-based transient effects. While we omit a plot, we note that total system angular momentum is also conserved in this simulation to within 0.02%. Lastly, select orbital parameters are computed and plotted in Fig. 6. The osculating orbit elements are computed without averaging using the evolving position and velocity of the primary and the barycenter of the secondary (e.g., Murray & Dermott (1999)). The orbital dynamics are not the focus of this study, but results are provided for completeness.

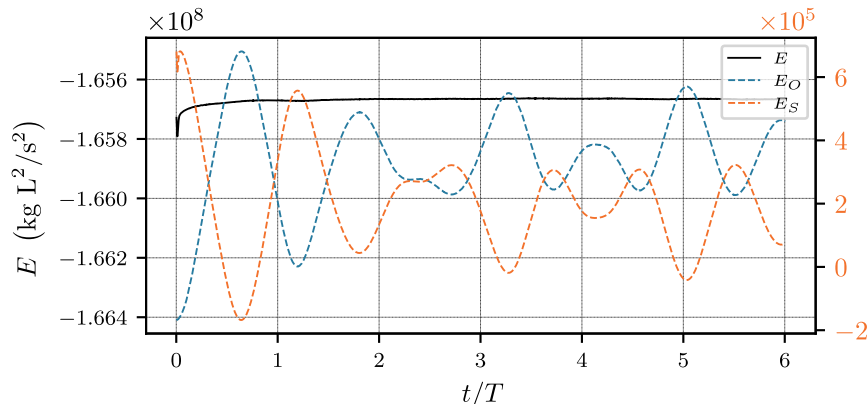


Figure 5: Total system energy, as computed by Eq. (10). This is furthermore factored into the classical orbital energy $E_O = \frac{1}{2}Mv_1^2 + \frac{1}{2}mv_2^2 - G\frac{Mm}{r}$ and the remaining energy of the secondary, $E_S = E - E_O$. For this case, the change in the secondary’s shape is minimal, so the rigid body-based energy estimation is conserved to within 0.1%. Note the difference of scales – most of the system energy resides in the orbit of the secondary. Here the effects of the initial transient behavior discussed in Section 2.2.2 can be seen as a brief dip and recovery in E .

3.2 Case 2: Super-synchronous rotation

Important simulation information is summarized in Table 2. The rubble pile secondary is initialized in a super-synchronous spin state, with the initial yaw rate (at the “zero” attitude state

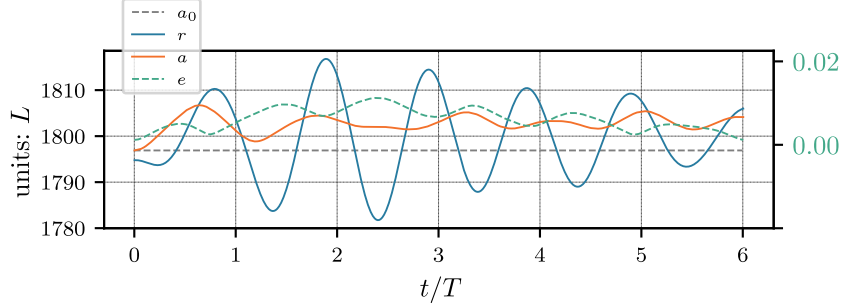


Figure 6: Select osculating orbital parameters of the secondary for the case of non-principal axis rotation. Orbit-attitude coupling produces the non-Keplerian variations.

with $\psi = \theta = \phi = 0$) equal to twice the initial mean motion. This is not a particularly fast super-synchronous spin rate – as the body rotates to a yaw angle of 90 degrees, the yaw rate decreases to around 1.6 times the mean motion rate. The other two angles remain nearly zero so it is appropriate to consider this problem as 2D in our subsequent tidal analysis. The attitude evolution is given in terms of Euler angles in Fig. 7a and in terms of the angular velocity of the \mathcal{B} frame with respect to \mathcal{O}' in Fig. 7b. Note the secular decrease of the z component of the angular velocity of the secondary, and the change in characteristic behavior.

Table 2: Simulation Parameters for Case 2

Parameter	Value
Gravitational constant G	$4.0172 \times 10^{-10} \text{ kg} \cdot \text{L}^3/\text{s}^2$
Primary and secondary mass	$M = 5.35073 \times 10^{11} \text{ kg}$, $m = 4.88306 \times 10^9 \text{ kg}$
Secondary number of particles	3046
Scaling parameter	1 m = 1.81904 L
Physical properties	Young’s mod. $Y = 3\text{GPa}$, Friction $\mu = 0.6$, Poisson $\nu = 0.3$
Initial attitude of secondary	$\psi = \theta = \phi = 0$
Initial angular velocity	$\boldsymbol{\omega}_2 = (0, 0, 2n_0) \text{ rad/s}$
Initial orbit elements	$a = 2145.1\text{L}$, $e = 2.8582 \times 10^{-3}$, $f = 0^\circ$
Timescales	$T_{\text{orbit}} \approx 12.0 \text{ hrs}$, $T_{\text{libration}} \approx 14.3 \text{ hrs}$

Fig. 7c gives the tidal torque about the x, y, z body axes of the binary secondary, as reproduced from the outputs of GRAINS. Because the secondary spin remains nearly coplanar with the orbit, the torque is dominated by the polar (z) term. The two red dots near the line of zero torque denote the z torque at the start and end of a full rotation (e.g. at two subsequent instances of $\psi = 0$), for use in later calculations. A strong agreement can be noted between the numerically recovered estimate of the tidal torque (dashed lines), Eq. (17), and the computation based on MacCullagh’s approximation (solid lines), Eq. (15). The polar torque shown is a sum of the conservative tidal torque $\Gamma_{z,\text{PMA}}$ and the dissipative tidal torque $\Gamma_{z,\text{Tidal}}$, and averaging over full rotations reveals a net negative (de-spinning) torque per rotation. This is to be used shortly for calculating the dissipativeness of the rubble pile. Fig. 7d gives the rotational energy of the secondary, as computed by Eq. 12, for the case of super-synchronous rotation. This energy quantity displays significant secular decrease over the course of the simulation. As with the NPA case, initial transience in \mathcal{E} is “washed out”. Lastly, the moments of inertia in the \mathcal{G} frame are plotted in Fig. 8. Note the transient initialization effects on the shape in the first fraction of an orbit, and the longer-term

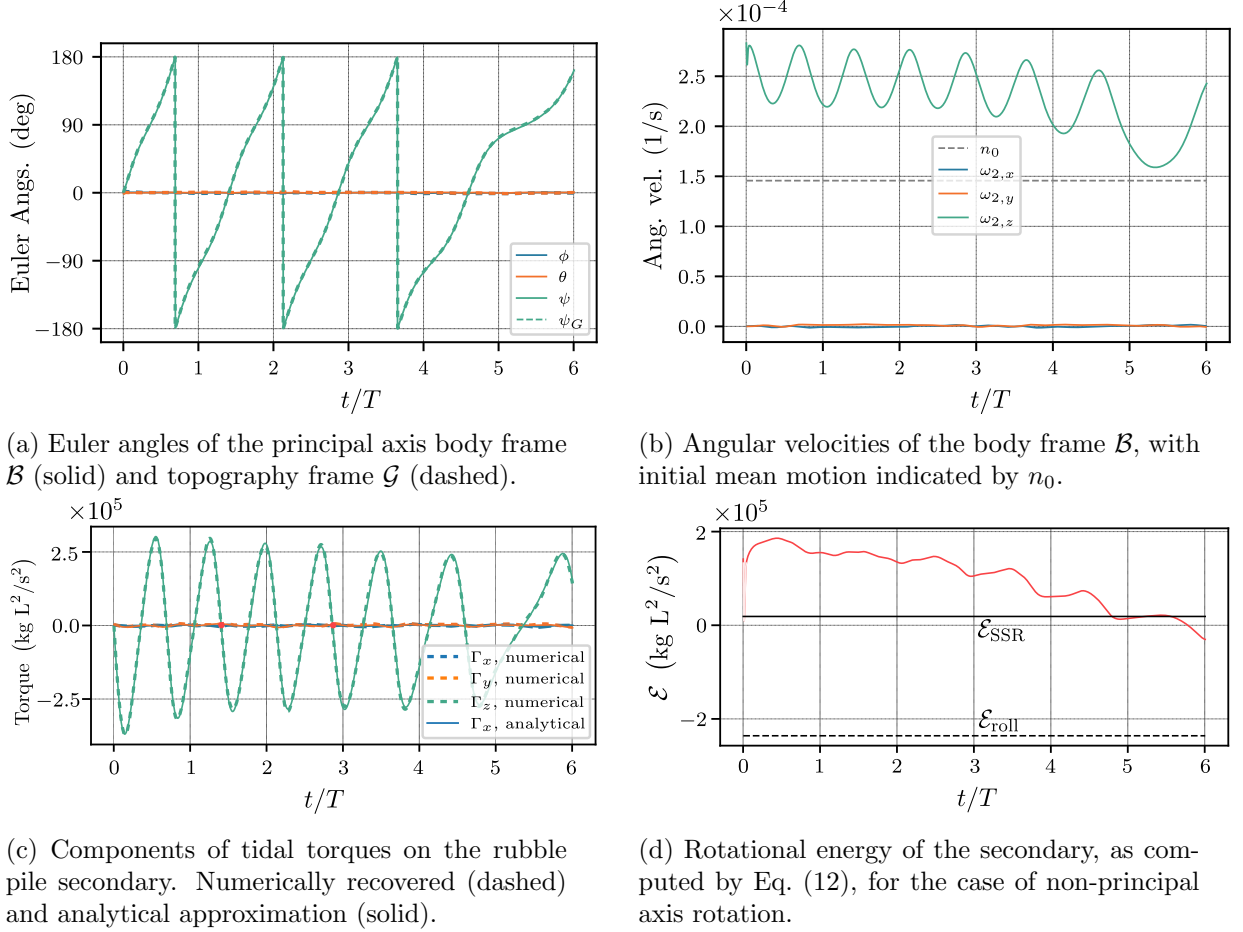


Figure 7: Simulation results for Case 2 (SSR). \mathcal{B} frame Euler angles (a) correspond to the rotation matrix $[\mathcal{B}\mathcal{O}']$, whereas \mathcal{G} corresponds to the rotation matrix $[\mathcal{G}\mathcal{O}']$. The angles indicate a primarily flat spin, coplanar with the orbit. The tidal torques (c) are provided in the \mathcal{B} frame. The two red dots near the line of zero torque $\Gamma_{(\cdot)} = 0$ denote the z torque at the start and end of a full rotation (e.g. at two subsequent instances of $\psi = 0$), for use in later calculations. Rotational energy (d) starts in a super-synchronous rotation case, as evidenced by $\mathcal{E} > \mathcal{E}_{\text{SSR}}$. Towards the end of the simulation, there is a predicted transition to bounded spin state. This transition is inexact because of the inherent assumptions in the derivation of \mathcal{E} limits.

settling of I_{zz} and I_{yy} due to spin-down. Such transience occupies $\sim 10\%$ of the first simulated orbit. Conservatively, we neglect the first full orbit in all of our tidal analysis.

3.3 Tidal Computations

3.3.1 Estimating Q/k_2

Given the successful recovery of a tidal torque signal, the equations outlined in Section 2.2 can be applied to estimate Q/k_2 and Q , as well as other parameters of interest, for the case of super-synchronous rotation. An attempt is also made to recover general 3D rotational analogs of these quantities for the non-principal axis rotation case. We start with a discussion of the

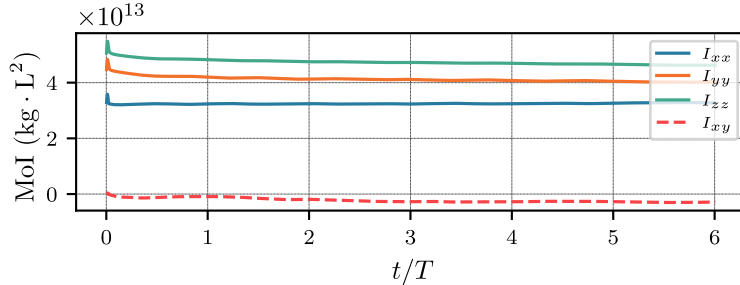


Figure 8: Select moments of inertia, \mathcal{G} frame. The small nonzero I_{xy} demonstrates that it is not a principal axis frame. Note the transient shape effects in the first $\sim 1/10$ of an orbit, and the longer-term settling of I_{zz} and I_{yy} due to spin-down – the rubble pile becomes slightly less oblate (plane perpendicular to z) and elongated (plane perpendicular to y).

super-synchronous rotation case because it is a planar case and thus closer to the classical theory.

Ignoring the first orbit to mitigate the effects of settling on our computations, we compute Q/k_2 using Eq. (22) for a number of revolutions of the secondary. We also obtain rough estimates of Q by applying Eq. (19) with Eq. (12). The results are given in Fig. 9, which also discusses additional details of computation. Note that times when Γ_z is zero do not correspond to the times when the long axis of the secondary is aligned with the radial direction, i.e. times when $\psi = 0$ or $k\pi$ for integer k . Nonetheless the difference between computation via averaging in rotation cycles vs. torque cycles is small, on the order of a few percent. The variations on Q/k_2 based on which interval (i.e. which full rotation) it’s computed in are much larger. Averaging over all intervals, we obtain $Q/k_2 \sim 43.5^{+36.0}_{-27.2}$, which is a rather dissipative result. Fig. 9 shows that there is a notable dependence of Q/k_2 on the spin rate $\omega_{2,z}$. Namely, the dissipativity increases as the secondary spins down and approaches the synchronous state. The classical MacDonald tidal model does not account for such a frequency dependence of the dissipativity. We don’t estimate k_2 from these two results (Q/k_2 and Q) because the governing dynamics are quite different from the assumptions of the MacDonald tidal model and thus we caution against “chaining” computation of parameters except directly from model observables.

Moving on to the non-principal axis rotation case, we apply Eq. (23) to estimate Q/k_2 . Applying this strategy to the SSR case, we note the numerical difference between the two computations is negligible, on the order of a fraction of a percent. This verifies a function that recovers the classical planar result but can be extended to the more general non-planar rotation case. The results are shown in Fig. 10. Neglecting the first full orbit to mitigate the influence of initialization transience effects on our computations, we perform a linear fit to approximate the secular decrease in $\|\mathbf{H}_2(t)\|$ for the NPA case. This result is used to estimate Q/k_2 , and we obtain $Q/k_2 \sim 54.9$, which fits well within the range of the ranges obtained for the SSR case despite the vastly different scenario. This result might suggest that the NPA case is similarly dissipative to the SSR case, but we caution that the choice of interval for the fit affects the computation. Neglecting for example the first 1/3 of the time, the resulting fit gives $Q/k_2 \sim 74.0$, which is a bit less dissipative. To provide an extreme example, fitting only the data from the latter half of the simulation, the slope of the linear fit to $\|\mathbf{H}_2(t)\|$ is actually positive, and thus Q/k_2 becomes undefined. The local minima and maxima of this plot are somewhat irregular in comparison to the SSR case, and cannot be used to ascertain a reasonable interval to compute Q/k_2 .

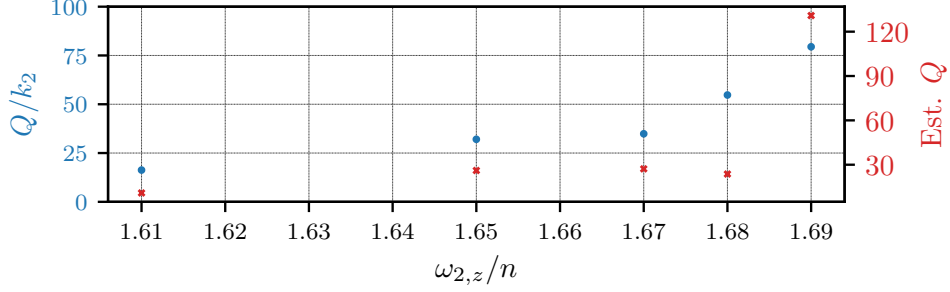


Figure 9: Calculated Q/k_2 , and roughly estimated Q , vs. interval-averaged normalized spin rate, $\omega_{2,z}/n$. These are computed across the following interval indices, traversing the plot from left to right: (7,11), (6,10), (5,9), (4,8), (3,7). Starting from zero, these indices count the zeros of Γ_z in Fig. 7c, where 4 zero crossings (and 4 maxima/minima) occur per rotation of the secondary, and the indices (4,8) are indicated in that figure with red dots.

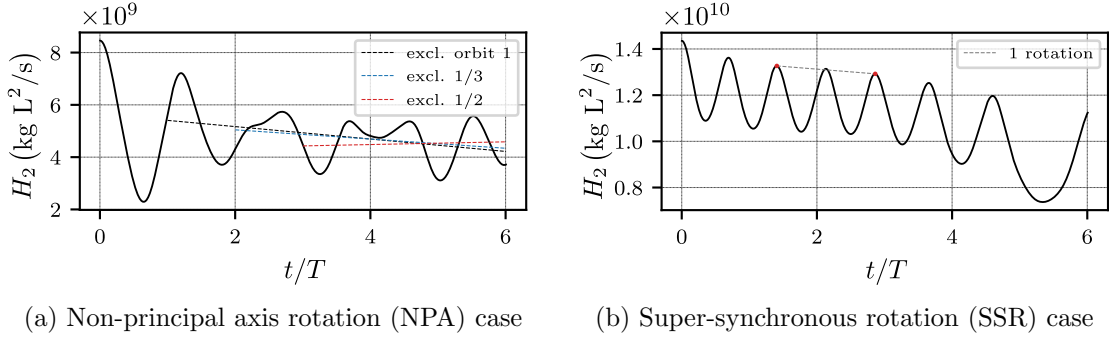


Figure 10: Estimating Q/k_2 for both cases using H_2 . For the SSR case, we apply Eqs. (22) and (23) and note close agreement between the two computations. The interval shown by the red dots corresponds to interval indices (4,8). See the details of Fig. 9. Every time $\psi = k\pi/2$ for integer k , it corresponds roughly to a local maxima or minima in H_2 . For the NPA case, this is done with secular fits of part of $H_2(t)$. The choice of interval affects the result using Eq. (23).

3.3.2 Direct Observation of the Semidiurnal Tide

Because GRAINS tracks the locations of individual mass elements of the rubble pile, it is possible to directly observe the semidiurnal tides from the simulation results in the SSR case. At a given topographic longitude on the secondary, twice per “day” (e.g. full rotation in ψ), there will be two high and low tides acting on the regolith, corresponding to times when the strength of the tides from the primary are at their local maximum and minimum. Switching to our topographic frame \mathcal{G} , we resolve the radial distance from the barycenter of a mass element on the surface along the equator. The result is shown in Fig. 11, which clearly depicts two local maxima and two local minima per day on the binary secondary. As the body spins down and approaches tidal locking, the global settling overwhelms this tidal effect, hence the qualitatively distinct behavior on Day 4.

We can confirm that the radial range variations of mass elements along the equator are indeed the semidiurnal tide by producing similar plots to Fig. 11 for a number of mass elements at different longitudes along the equator, recording the timing of the local maxima, and stacking these variations by longitude. The result is given in Fig. 12. This figure shows that the timing of high tide varies

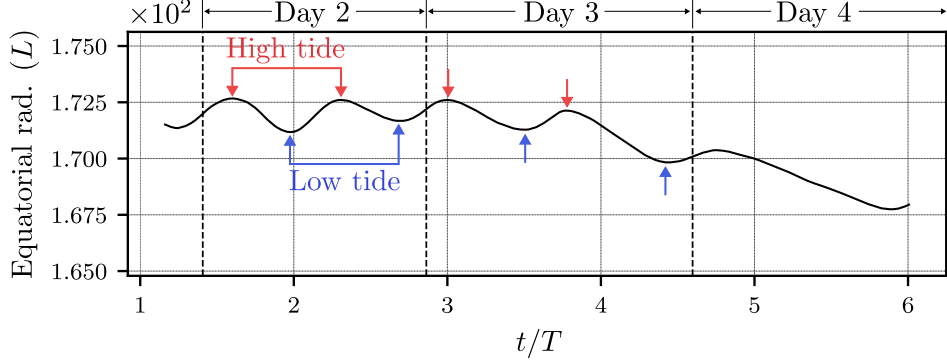


Figure 11: Radial distance of a mass element from the barycenter computed over time, longitude $\varphi = 168^\circ$. Local maxima are marked with red arrows, and local minima with blue. In the final rotation, where the spin rate decreases significantly, there is significant equatorial radial settling.

predictably as a function of longitude (similar to how the timing of the lunar semidiurnal tide varies based on longitude on the Earth), revealing the global extent of the tide. From the horizontal distance between high tide markers and the horizontal dashed lines (representative of the response of a completely non-dissipative body), the temporal lag of the semidiurnal tide can be inferred. Note that it is not a constant function of longitude (another result defying the simple MacDonald model). Furthermore, comparing the temporal lags across Days 2 and 3, we can discern that this lag is also a function of spin rate $\omega_{2,z}$. This result is to be expected based on the previously obtained result of Q/k_2 varying as a function of $\omega_{2,z}$. Lastly, the tidal strain varies, in the range $10^{-4} \lesssim \frac{H}{R} \lesssim 10^{-3}$ for radial variations H and local equatorial radius R .

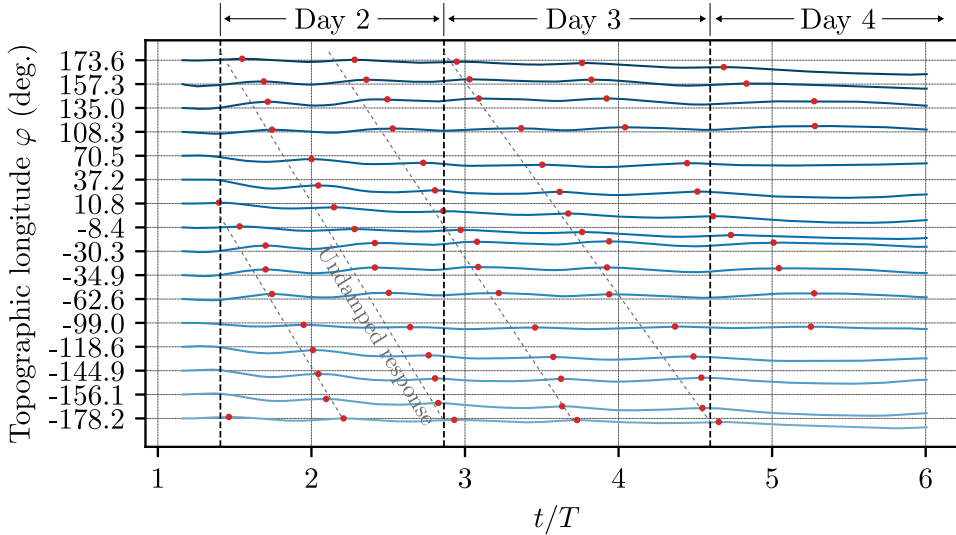


Figure 12: Timing of semidiurnal high tide vs. longitude. For select longitudes along the equator, the radial distance of a mass element from the barycenter is computed over time. Local maxima are marked with red dots, revealing a global order-2 pattern. The gray lines approximate mean timings of high tide for a perfectly elastic body whose response to the tidal forcing is instantaneous. Tidal temporal lag can be visualized via the horizontal distance from the high tide points to the nearby diagonal lines. Note the dependence on longitude φ and on time (or relatedly, spin rate $\omega_{2,z}$).

4 Discussion

Conducting a study of spin-down from a planar super-synchronous spin state, we obtain $Q/k_2 \sim 43.5_{-27.2}^{+36.0}$, which is a rather dissipative result. As a point of comparison, a recent study by Pou & Nimmo (2024) gives estimated ranges of $10^2 < Q_s/k_{2,s} < 10^6$ for about a dozen binary secondaries. That work, however, makes use of observational studies of implied historical orbital evolution (for estimating $Q_p/k_{2,p}$ for the primary) or implied historical spin evolution (for estimating $Q_s/k_{2,s}$ for the secondary). In such a study, it is difficult to parse out the effects of BYORP and YORP, respectively, from a Q/k_2 purely tied to effective “rheology”, which is what is provided here. For short-timescale processes such as tidal locking of the secondary, numerically derived estimates of the dissipativity, such as the computations explored in this work, could have superior precision to astrometry – providing not only upper or lower bounds for parameters of interest, but precise numerical values, with the possibility to explore the underlying physics. However, as mentioned, more information is needed regarding how parameters such as the distribution of particle sizes and the shape of the secondary affect the numerical results. We simply provide a numerical recipe for conducting numerical studies of tidal dissipation in binary systems, but the results are compelling.

We also remind the reader of the recent work by DellaGiustina et al. (2024). Our setup is quite different, with a larger particle budget, the use of non-spherical mass elements, their split of mass elements across both bodies vs. our concentration of all mass elements into the secondary, and their focus on the dissipation within the primary vs. ours on rotational settling of the secondary. We also note that in comparison to our results, their orbit radius seems more regular, perhaps due to the less nonspherical secondary. In contrast to our quality factor estimates roughly estimated from the change in rotational energy \mathcal{E} , they apply the formula $Q_{\text{tide}} = (2\Delta t|\omega_1 - n|)^{-1}$ (Efroimsky & Lainey, 2007) for primary rotation rate ω_1 and orbital mean motion n , and temporal lag Δt . Their result of $Q_{\text{tide}} = 8.97$, for the primary, was an order of magnitude smaller than prior estimates for monoliths (Goldreich & Sari, 2009), and also is a bit lower than our roughly estimated values of $Q \sim 30$, although again computed for a different body via a different approach. This agrees with our observation that rubble piles, when simulated numerically, are highly dissipative.

The possibility of binary asteroid systems being on the more dissipative side of prior estimates in literature, as suggested by this work, would have big implications for the scientific community, including for the upcoming Hera mission to study the aftermath of the DART impact on Dimorphos. Pravec et al. (2024) found, via lightcurve analysis, that the DART mission likely put Dimorphos in a fairly excited attitude state, with large (though probably bounded) yaw angles, and the possibility for unbounded roll, though poorly constrained by the lightcurve analysis. Recall that unbounded roll was reached as an eventual spin state in our simulation initialized in a spin state with large yaw and pitch rates. Our simulation also computed an effective Q/k_2 low enough to be comparable to the values obtained for the super-synchronous case, but we note that the choice of averaging interval affected the result. If this low Q/k_2 result, conducted in the NPA simulation of a Didymos-Dimorphos system, can be trusted, perhaps when the Hera mission arrives at the Didymos system in late 2026, it will find Dimorphos in a more settled state than previously anticipated. We make no quantitative predictions in this exploratory work. At a minimum, we demonstrate that further study with high-fidelity modeling is needed to determine the nature of the disagreement between these numerical results and the estimates of Q/k_2 obtained by means of scaling analysis and astrometry. There are also various inconsistencies within the literature. Nimmo & Matsuyama (2019) argues for shallow friction-dominated dissipation, whereas Goldreich & Sari (2009) argues for dissipation dominated by yielding at sharp points on rocks in the asteroid interior. In the viewpoint of the latter, effective rigidity becomes dynamically important for dissipation, whereas Efroimsky

(2015) instead argues that effective viscosity is much more important than effective rigidity. Such theoretical disputes can and should be resolved by numerical study.

The rubble pile secondary, when initialized, exhibits a brief transient response in the start of the simulation as it settles towards a more equilibrium shape. This is notable from the short spike in the very start of Figure 8. We find that this happens rather quickly, in agreement with the findings of Tanga et al. (2009), which by contrast was conducted in `pkdgrav` with smooth spheres. This issue is just one of many implementational details that we discuss for conducting scientific studies of tidal dissipation in discrete element models. We note also that our finding that rubble piles are quite dissipative is in agreement with a finding of Wimarsson et al. (2024) that some of the aggregating “moonlets” in binary asteroid systems tidally lock extremely quickly, in a timespan of days. That study was also conducted in `GRAINS`.

For longer-term numerical studies, our suggested workflow is to carefully and rigorously combine high- and low-fidelity (e.g. non- N body) models. Short-duration high-fidelity simulations, such as the ones conducted in this work, can be used provide estimated tidal parameters for scenarios of interest based on orbit/body sizes, body shape, and spin states. Then, a faster simulation architecture, modeling only the rigid-body physics (Davis & Scheeres, 2020), plus various parametric equations for YORP and tides, is loaded with an approximate tidal torque which is adjusted as needed based on the spin/orbit regime. See e.g. Cueva et al. (2024) for a recent study. However, we caution against blind implementation of the MacDonald tidal torque model, because even small changes to the unimodal model assumptions, beyond the MacDonald case (e.g., Williams & Efroimsky (2012)), can produce quite different outcomes in long-term numerical simulations. This was noted, for example, in a recent study with long-term simulations of the tidal settling of Europa (E. R. Burnett & Hayne, 2023). There is also the fact that a unimodal tidal model, with associated fixed lag angle, may not be a sufficient approximation of the tidal physics captured in high-fidelity models such as in this work. This can be discerned from the significant variations in temporal lag of the tidal bulge as seen in Figure 12. A far superior choice would be the development of distinct low-fidelity tidal models specifically for rubble pile asteroids, which are designed to serve as valid first-order approximations of the high-fidelity physics as revealed by `GRAINS` or alternate N -body models.

5 Conclusions

In this work we outline a numerical recipe for conducting detailed studies of tidal dissipation in N -body models of rubble pile binary systems, and apply the result to a system similar in size, scale, and geometry to Didymos-Dimorphos. Focusing on tidal dissipation in the secondary, we render the primary as a point mass so that all remaining particles in the N -body model can be used to build the secondary. Key results from this study include the successful emergence and identification of tidal distortion, tidal lag, and resulting dissipation. This is the first study to our knowledge to rigorously estimate the resulting dissipativity of the rubble pile binary secondary from an N -body model. We obtain a highly dissipative result of $Q/k_2 \sim 43.5^{+36.0}_{-27.2}$, specifically for Dimorphos, which is on/below the low end for binary secondaries predicted by various other studies. We note that the effect of size distribution of the constitutive particles on dissipativity should be explored. We introduce a number of helpful strategies needed for conducting further numerical studies. These include the definition of a novel “topography” frame, fixed with respect to select rocks deep in the interior, the identification and exclusion of initial transient behaviors inherent to numerical rubble pile models, and outlining numerical computations, based in classical theory, for estimating various

tidal quantities of interest. In our view, the current use of classical first-order unimodal viscoelastic tidal theory with binary systems is of limited accuracy/relevance, given the appearance of extensive non-classical tidal behaviors in our numerical simulation. We advocate for supplementary studies relying on numerical (and also in-laboratory) experiments, focused on the goal of improving our fundamental understanding of the underlying physics of dissipation in rubble piles. This work is an important step towards a true and holistic understanding of such systems.

6 Disclaimer

Funded/co-funded by the European Union (Horizon Europe, FFAST-MSCA, 101063274; ERC, TRACES, 101077758). Views and opinions expressed are however those of the authors only and do not necessarily reflect those of the European Union, the European Research Executive Agency, or the European Research Council. Neither the European Union nor the granting authority can be held responsible for them.

References

- Agrusa, H. F., Ferrari, F., Zhang, Y., Richardson, D. C., & Michel, P. (2022, Jul.). Dynamical Evolution of the Didymos-Dimorphos Binary Asteroid as Rubble Piles following the DART Impact. *The Planetary Science Journal*, 3(7), 158. doi: 10.3847/PSJ/ac76c1
- Agrusa, H. F., Gkolias, I., Tsiganis, K., Richardson, D. C., Meyer, A. J., Scheeres, D. J., . . . Davis, A. B. (2021, Dec.). The excited spin state of Dimorphos resulting from the DART impact. *Icarus*, 370, 114624. doi: 10.1016/j.icarus.2021.114624
- Bottke, W. F., Vokrouhlický, D., Rubincam, D. P., Brož, M., & Gehrels, T. (2002). The Effect of Yarkovsky Thermal Forces on the Dynamical Evolution of Asteroids and Meteoroids. In *Asteroids III* (pp. 395–408). University of Arizona Press. doi: 10.2307/j.ctv1v7zdn4.32
- Burnett, E., Fodde, I., & Ferrari, F. (2024, Sep.). Numerical inference of viscoelastic properties in tidal models of rubble pile asteroids. In *EGU General Assembly*. Vienna, Austria. doi: 10.5194/egusphere-egu24-17927
- Burnett, E. R., Fodde, I., & Ferrari, F. (2024, Sep.). Enhanced tidal dissipation in rubble pile binary secondaries revealed via numerical studies. In *Europlanet science congress*. Berlin, Germany. doi: 10.5194/epsc2024-1174
- Burnett, E. R., & Hayne, P. O. (2023, Dec.). Spin–orbit coupling of Europa’s ice shell and interior. *Icarus*, 406, 115731. doi: 10.1016/j.icarus.2023.115731
- Cueva, R. H., McMahon, J. W., Meyer, A. J., Scheeres, D. J., Hirabayashi, M., Raducan, S. D., . . . Merrill, C. C. (2024, Feb). The Secular Dynamical Evolution of Binary Asteroid System (65803) Didymos Post-DART. *The Planetary Science Journal*, 5(2), 48. doi: 10.3847/PSJ/ad2173
- Čuk, M., & Burns, J. A. (2005, Aug.). Effects of thermal radiation on the dynamics of binary NEAs. *Icarus*, 176(2), 418–431. doi: 10.1016/j.icarus.2005.02.001
- Daly, R. T., Ernst, C. M., Barnouin, O. S., Chabot, N. L., Rivkin, A. S., Cheng, A. F., . . . Zhang, Y. (2023, Mar.). Successful kinetic impact into an asteroid for planetary defence. *Nature*, 616(7957), 443–447. doi: 10.1038/s41586-023-05810-5

- Daly, R. T., Ernst, C. M., Barnouin, O. S., Gaskell, R. W., Nair, H., Agrusa, H., ... LICIACube teams (2024, Jan.). An Updated Shape Model of Dimorphos from DART Data. *The Planetary Science Journal*, 5(1), 24. doi: 10.3847/PSJ/ad0b07
- Davis, A. B., & Scheeres, D. J. (2020, May). Doubly synchronous binary asteroid mass parameter observability. *Icarus*, 341, 113439. doi: <https://doi.org/10.1016/j.icarus.2019.113439>
- DellaGiustina, D. N., Ballouz, R. L., Walsh, K. J., Marusiak, A. G., Bray, V. J., & Bailey, S. H. (2024, Feb.). Seismology of rubble-pile asteroids in binary systems. *Monthly Notices of the Royal Astronomical Society*, 528(4), 6568-6580. doi: 10.1093/mnras/stae325
- Efroimsky, M. (2012, March). Bodily tides near spin-orbit resonances. *Celestial Mechanics and Dynamical Astronomy*, 112, 283-330. doi: 10.1007/s10569-011-9397-4
- Efroimsky, M. (2015, Sep.). Tidal Evolution Of Asteroidal Binaries. Ruled By Viscosity. Ignorant Of Rigidity. *The Astronomical Journal*, 150(4), 98. doi: 10.1088/0004-6256/150/4/98
- Efroimsky, M., & Lainey, V. (2007, Dec.). Physics of bodily tides in terrestrial planets and the appropriate scales of dynamical evolution. *Journal of Geophysical Research: Planets*, 112(E12). doi: 10.1029/2007JE002908
- Ferrari, F., Lavagna, M., & Blazquez, E. (2020, Feb.). A parallel-GPU code for asteroid aggregation problems with angular particles. *Monthly Notices of the Royal Astronomical Society*, 492(1), 749-761. doi: 10.1093/mnras/stz3458
- Ferrari, F., Raducan, S. D., Soldini, S., & Jutzi, M. (2022, Jul). Ejecta Formation, Early Collisional Processes, and Dynamical Evolution after the DART Impact on Dimorphos. *The Planetary Science Journal*, 3(7), 177. doi: 10.3847/PSJ/ac7cf0
- Ferrari, F., & Tanga, P. (2022, May). Interior of top-shaped asteroids with cohesionless surface. *Icarus*, 378, 114914. doi: 10.1016/j.icarus.2022.114914
- Ferrari, F., Tasora, A., Masarati, P., & Lavagna, M. (2017). N-body gravitational and contact dynamics for asteroid aggregation. *Multibody System Dynamics*, 39(1), 3-20. doi: 10.1007/s11044-016-9547-2
- Fleischmann, J. A. (2015). *DEM-PM Contact Model with Multi-Step Tangential Contact Displacement History* (Tech. Rep.). Simulation-Based Engineering Laboratory, University of Wisconsin-Madison. Retrieved from <https://api.semanticscholar.org/CorpusID:16632649>
- Frouard, J., Quillen, A. C., Efroimsky, M., & Giannella, D. (2016, Mar.). Numerical simulation of tidal evolution of a viscoelastic body modelled with a mass-spring network. *Monthly Notices of the Royal Astronomical Society*, 458(3), 2890-2901. doi: 10.1093/mnras/stw491
- Goldreich, P., & Peale, S. (1966, Aug.). Spin-orbit coupling in the solar system. *The Astronomical Journal*, 71(6), 425-437. doi: 10.1086/109947
- Goldreich, P., & Sari, R. (2009, Jan.). Tidal Evolution of Rubble Piles. *The Astrophysical Journal*, 691, 54-60. doi: 10.1088/0004-637X/691/1/54
- Hestroffer, D., Sánchez, P., Staron, L., Bagatin, A. C., Eggl, S., Losert, W., ... Yano, H. (2019). Small Solar System Bodies as granular media. *The Astronomy and Astrophysics Review*, 27(1), 6. doi: 10.1007/s00159-019-0117-5

- Holsapple, K. A. (2010, Feb.). On YORP-induced spin deformations of asteroids. *Icarus*, *205*(2), 430-442. doi: 10.1016/j.icarus.2009.08.014
- Hou, X., Scheeres, D. J., & Xin, X. (2017). Mutual potential between two rigid bodies with arbitrary shapes and mass distributions. *Celestial Mechanics and Dynamical Astronomy*, *127*(3), 369–395. doi: 10.1007/s10569-016-9731-y
- Jacobson, S. A., Scheeres, D. J., & McMahon, J. (2013, Dec.). Formation of the Wide Asynchronous Binary Asteroid Population. *The Astrophysical Journal*, *780*(1), 60. doi: 10.1088/0004-637X/780/1/60
- Marti, J., Quinteros, S., Mikesell, D., Margerin, L., Delage, P., & Murdoch, N. (2024, Sep.). An experimental study of the influence of regolith micro-structure on seismic wave velocities. In *Europlanet science congress*. Berlin, Germany. doi: 10.5194/epsc2024-488
- Melosh, H. J. (2011). *Planetary surface processes*. Cambridge University Press. doi: 10.1017/CBO9780511977848
- Michel, P., Küppers, M., Bagatin, A. C., Carry, B., Charnoz, S., de Leon, J., ... Carnelli, I. (2022, Jul.). The ESA Hera Mission: Detailed Characterization of the DART Impact Outcome and of the Binary Asteroid (65803) Didymos. *The Planetary Science Journal*, *3*(7), 160. doi: 10.3847/PSJ/ac6f52
- Murray, C. D., & Dermott, S. F. (1999). *Solar System Dynamics*. Cambridge University Press. doi: 10.1017/CBO9781139174817
- Nimmo, F., & Matsuyama, I. (2019, Mar.). Tidal dissipation in rubble-pile asteroids. *Icarus*, *321*, 715-721. doi: 10.1016/j.icarus.2018.12.012
- Pou, L., & Nimmo, F. (2024, March). Tidal dissipation of binaries in asteroid pairs. *Icarus*, *411*, 115919. doi: 10.1016/j.icarus.2023.115919
- Pravec, P., Meyer, A., Scheirich, P., Scheeres, D., Benson, C., & Agrusa, H. (2024). Rotational lightcurves of Dimorphos and constraints on its post-DART impact spin state. *Icarus*, *418*, 116138. doi: 10.1016/j.icarus.2024.116138
- Pravec, P., Scheirich, P., Kušnirák, P., Hornoch, K., Galád, A., Naidu, S., ... LaCluyze, A. (2016). Binary asteroid population. 3. Secondary rotations and elongations. *Icarus*, *267*, 267-295. doi: 10.1016/j.icarus.2015.12.019
- Pravec, P., Scheirich, P., Kušnirák, P., Šarounová, L., Mottola, S., Hahn, G., ... Kober, G. (2006). Photometric survey of binary near-Earth asteroids. *Icarus*, *181*(1), 63-93. doi: 10.1016/j.icarus.2005.10.014
- Raducan, S. D., Jutzi, M., Cheng, A. F., Zhang, Y., Barnouin, O., Collins, G. S., ... May, B. H. (2024). Physical properties of asteroid Dimorphos as derived from the DART impact. *Nature Astronomy*, *8*(4), 445–455. doi: 10.1038/s41550-024-02200-3
- Richardson, D. C., Walsh, K. J., Murdoch, N., & Michel, P. (2011). Numerical simulations of granular dynamics: I. Hard-sphere discrete element method and tests. *Icarus*, *212*(1), 427-437. doi: 10.1016/j.icarus.2010.11.030
- Rubincam, D. P. (2000). Radiative Spin-up and Spin-down of Small Asteroids. *Icarus*, *148*(1), 2-11. doi: 10.1006/icar.2000.6485

- Sánchez, P., & Scheeres, D. J. (2014, May). The strength of regolith and rubble pile asteroids. *Meteoritics & Planetary Science*, *49*(5), 788-811. doi: 10.1111/maps.12293
- Scheeres, D. (2007, Aug.). Rotational fission of contact binary asteroids. *Icarus*, *189*(2), 370-385. doi: 10.1016/j.icarus.2007.02.015
- Tanga, P., Comito, C., Paolicchi, P., Hestroffer, D., Cellino, A., Dell’Oro, A., . . . Delbo, M. (2009). Rubble-Pile Reshaping Reproduces Overall Asteroid Shapes. *The Astrophysical Journal*, *706*(1), L197-L202. doi: 10.1088/0004-637X/706/1/L197
- Tasora, A., Serban, R., Mazhar, H., Pazouki, A., Melanz, D., Fleischmann, J., . . . Negrut, D. (2016). Chrono: An Open Source Multi-physics Dynamics Engine. In T. Kozubek, R. Blaheta, J. Šístek, M. Rozložník, & M. Čermák (Eds.), *High performance computing in science and engineering* (pp. 19–49). Cham: Springer International Publishing. doi: 10.1007/978-3-319-40361-8_2
- Thomas, C. A., Naidu, S. P., Scheirich, P., Moskovitz, N. A., Pravec, P., Chesley, S. R., . . . Agrusa, H. F. (2023). Orbital period change of Dimorphos due to the DART kinetic impact. *Nature*, *616*(7957), 448–451. doi: 10.1038/s41586-023-05805-2
- Walsh, K. J., Richardson, D. C., & Michel, P. (2012). Spin-up of rubble-pile asteroids: Disruption, satellite formation, and equilibrium shapes. *Icarus*, *220*(2), 514-529. doi: 10.1016/j.icarus.2012.04.029
- Williams, J. G., & Efroimsky, M. (2012). Bodily tides near the 1:1 spin-orbit resonance: correction to Goldreich’s dynamical model. *Celestial Mechanics and Dynamical Astronomy*, *114*, 387–414. doi: 10.1007/s10569-012-9446-7
- Wimarsson, J., Xiang, Z., Ferrari, F., Jutzi, M., Madeira, G., Raducan, S. D., & Sánchez, P. (2024). Rapid formation of binary asteroid systems post rotational failure: A recipe for making atypically shaped satellites. *Icarus*, *421*, 116223. doi: 10.1016/j.icarus.2024.116223